ELSEVIER

Finite-size effects in the 3D reconstruction and morphological analysis of porous polymers

Tibor Müllner[1], Armin Zankel[2], Frantisek Svec[3] and Ulrich Tallarek[1,*]

[1] Department of Chemistry, Philipps-Universität Marburg, Hans-Meerwein-Strasse, 35032 Marburg, Germany
[2] Institute for Electron Microscopy, Graz University of Technology, and Center for Electron Microscopy Graz, Steyrergasse 17, 8010 Graz, Austria
[3] The Molecular Foundry, E.O. Lawrence Berkeley National Laboratory, 1 Cyclotron Rd., Berkeley, CA 94720-1460, United States

The morphology of porous polymers determines their transport characteristics and thus their efficiency in numerous applications. Tailoring the properties of a structure to the intended use presents a major challenge to materials scientists, as long as methods for an accurate morphological characterization are lacking. We demonstrate the large-volume reconstruction and analysis of a polymeric monolith using serial block face scanning electron microscopy. Skeleton and void space of the monolith are statistically evaluated to extract key structural parameters relevant to mass transport, and to quantify finite-size effects, which are usually neglected, on their values.

Introduction

Quantitative relationships between the morphology of a porous material and its local as well as global transport properties are important in several research areas, thereby addressing characteristic length scales from nanometers, as with catalyst nanoparticles [1,2], up to environmental fields, for example, in soil science [3–8]. Polymer-based materials with tailored micron and submicron morphological features are intensively used due to their low cost and flexible surface chemistry [9–13]. Porous polymeric scaffolds can nowadays be prepared with a hierarchy of micro-, meso-, and macroporous spatial domains [14–19]. The morphology of a material determines its transport characteristics and thus its efficiency in catalysis [20–22], fuel cell design [23,24], battery and electrode development [25–30], separation science [31–33], or selective gas extraction and storage [34–37]. For example, mass transport to and from the active surface sites in micropores and mesopores is usually purely diffusive and may limit reaction rates in technical catalysis [38–40].

Tailoring the properties of stationary supports to their intended use is a major challenge for materials scientists, as long as methods for their accurate and quantitative morphological characterization are lacking. The establishment of quantitative morphology-transport relationships may rely on direct pore-scale simulations of flow, mass, and charge transport in the 3D reconstruction of the material [41]. However, the simulations can only be as accurate as the underlying model permits. Acquiring a 3D reconstruction for materials with micron and submicron morphological features usually involves electron microscopy [42]. While scanning electron microscopy (SEM) and transmission electron microscopy (TEM) are both reliable and fast and therefore well suited for convenient screenings, the obtained information is only 2D and therefore limited. Since 2D cross-sections can be insufficient to capture the morphological features of a material [43], and also because of fundamental differences in the transport properties of 2D and 3D models [44–46], 3D imaging techniques are required to provide the essential morphological data and the full 3D model for realistic transport simulations.

From a portfolio of available methods [42,43,47–54], focused ion beam SEM (FIB-SEM) has become the dominating method for this task over the last years, since it is widely available, robust, and versatile with respect to the investigated material [24,55–61]. A drawback is the limited sample volume that can be covered in a reasonable time. As a result, the 3D reconstructions often show finite-size effects, which are manifested as the deviation of a measure from the global value due to the artificial spatial restrictions generated by the imaging process. Substantial effort has been dedicated to resolve this issue [6,8,59,62–65] but the actual volume necessary to derive the global value of a morphological parameter

*Corresponding author:. Tallarek, U. (tallarek@staff.uni-marburg.de)

1369-7021/ http://dx.doi.org/10.1016/j.mattod.2014.07.003

Please cite this article in press as: T. Müllner, et al., Mater. Today (2014), http://dx.doi.org/10.1016/j.mattod.2014.07.003

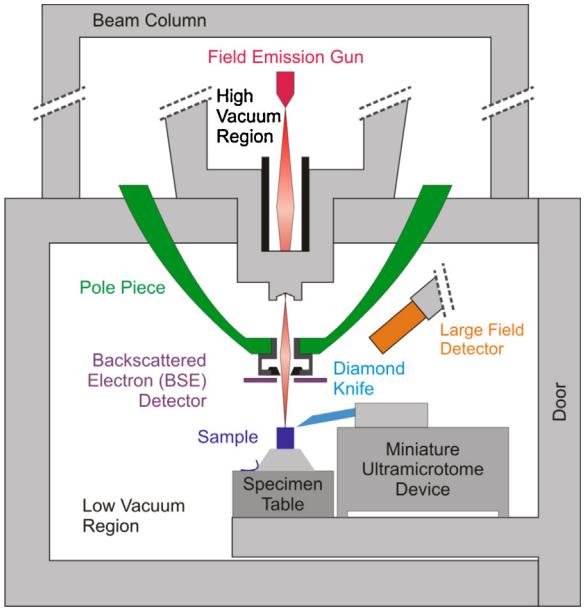

FIGURE 1

Setup of the serial block face scanning electron microscope, the combination of an environmental scanning electron microscope and an automated ultramicrotome located inside the specimen chamber. While most often the backscattered electron detector is used, the application of any detector compatible with environmental scanning electron microscopy is possible, including the popular secondary electron detector. The presence of an imaging gas in the low vacuum region compensates for charging effects, allowing to image without need for a sputter coating.

strongly depends on the measure of interest; it may address geometrical parameters such as porosity and void volume distributions, characteristic lengths and related heterogeneities, or topological measures such as pore interconnectivity.

Here we demonstrate with a large-volume reconstruction (~100 μm edge length) of a porous polymeric laboratory sample how finite-size effects can be evaluated and avoided. For this purpose, we employed serial block face SEM (SBF-SEM), a technique introduced by Denk and Horstmann in 2004 [66]. While their landmark paper and the subsequent commercialization by Gatan Inc. stimulated intense research in the life sciences, applications of this method in materials science are rare but promising [67–71]. Setup and working principle of SBF-SEM are illustrated in Figs 1 and 2, respectively. The powerful, yet simple combination of *in situ* ultramicrotomy and SEM offers the possibility to image large volumes of a material in a reasonable time, with the minor limitation that the specimen must be sliceable by a diamond knife.

Sample pretreatment and imaging

As the porous polymeric sample we used a hypercrosslinked poly(styrene-divinylbenzene) monolith confined in a cylindrical fused-silica capillary of 100 μm inner diameter. Preparation of the monolith was carried out following a literature procedure [72]. The material can be imaged over the whole cross-section of the capillary, which yields a physical confinement for the lateral dimension of the volume to be reconstructed. In addition, the capillary facilitates handling, especially during sample pretreatment. Since the sample consists of porous soft-matter, we increased its mechanical stability against possible damages during cutting, as observed in TEM slices [73], by filling the interstitial void space with an epoxy-type resin. It also allows for depth discrimination, which improves localization of solid phase (monolith skeleton) and void space (pores) in the obtained images. A drawback of the filling with resin is the loss of contrast, which requires a proper staining procedure. The capillary column format of the sample allowed us to perform these two steps with conventional laboratory equipment, simplifying standard immersion-based methods. Staining was achieved by overnight purging the sample with an aqueous solution of 4% (w/w) osmium tetroxide. Excess staining agent was removed by washing with pure water. After drying the sample, commercial SpeciFix-40 resin was used to

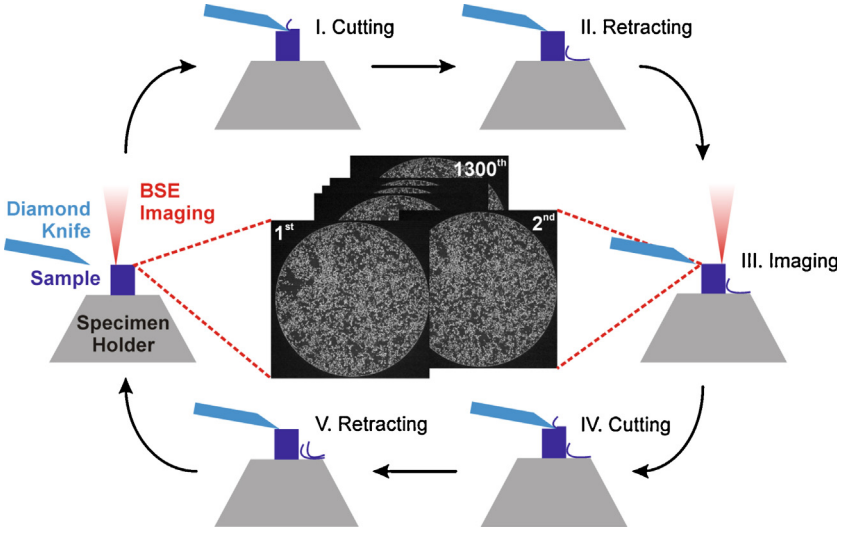

FIGURE 2

Working principle in serial block face scanning electron microscopy. A slice is cut from the sample, generating a clean and smooth surface on the block, which is then imaged. After imaging a new slice is removed from the sample block, yielding a new surface to be imaged. This cycle is repeated until the desired number of images is obtained. Typical slice thickness is in the range of 30–100 nm; lateral resolution corresponds to that of a standard scanning electron microscope.

Please cite this article in press as: T. Müllner, et al., Mater. Today (2014), http://dx.doi.org/10.1016/j.mattod.2014.07.003

fill interstitial void space within the monolith. This resin was chosen to ensure proper embedding. Its low viscosity allows infiltration without damaging or altering the structure. Like most epoxy-type resins it shows negligible shrinkage, notable by the absence of gaps at the polymer–silica interface and voids in the cured resin. Since the average pore size is a few micrometers [72], a modest pressure was applied to introduce the fast curing resin in the pores. After thermal curing, the fused-silica capillary wall was removed by immersing the sample in hydrofluoric acid. A secondary embedding in common flat embedding molds was performed, which finally yielded a mechanically stable sample with good handling properties.

The sample was then prepared for the electron microscopy imaging. First, a small cuboid of ca. 500 μm edge length was cut from the sample. This cuboid was attached to the specimen holder and a clean surface was cut using a conventional microtome equipped with a diamond knife. The specimen was transferred to the specimen chamber of an environmental scanning electron microscope followed by SBF-SEM measurements as illustrated in Fig. 2. In total, 1300 slices were obtained, each representing a thickness of 100 nm and consisting of 4000 × 4000 pixels (voxel: 29 nm × 29 nm × 100 nm). Imaging was performed with water vapor at about 107 Pa as imaging gas in backscattered electron mode, at an electron energy of 4 keV. Images were first binarized using an automated sequence consisting of image denoising, filtering, and thresholding. Afterwards, images were aligned along the column axis and duplicates (resulting from the fact that after several 100 cuts the diamond knife and sample mount had to be cleaned and a new stack to be started) were removed. This produced 1282 binary images altogether, representing a capillary column volume of 1.01×10^6 μm^3, while the actually imaged volume is 1.73×10^6 μm^3 (the difference is due to the circular cross-section of the column). Images were then stacked together to give a representation of the 3D monolith structure shown in Fig. 3.

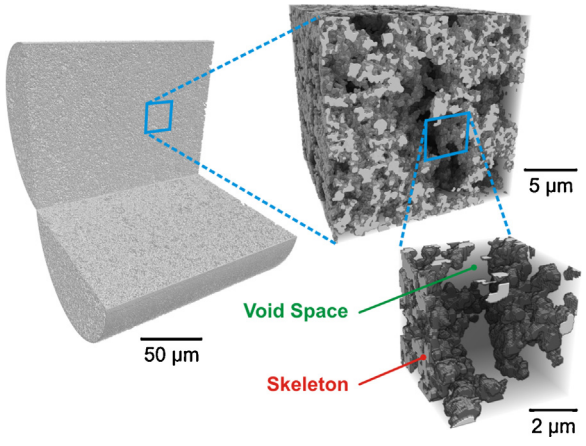

FIGURE 3

3D representation of the reconstructed cylindrical sample volume. In total, a monolith segment of 100 μm diameter and ~130 μm length was imaged and reconstructed. To give an impression of the monolith morphology and relevant length scales two cubic subvolumes, with edge lengths of 20 μm and 5 μm, are extracted and shown separately. The investigated specimen consists of a continuous polymeric structure (monolith skeleton; opaque) with a porosity of ~69% (interstitial void space; shaded).

Porosity analysis

Porosity (void volume fraction) and its distribution throughout the sample is a feature with enormous impact on the flow and mass transport properties of a material [74]. The porosity can be determined from the number of black pixels, which mark the pore (void) space, divided by the total number of pixels in the structure. This measure is also easily accessible as a global parameter with simpler and faster methods like pycnometry, flow porometry [75,76], mercury intrusion porosimetry [77–80], and many more [81,82]. The advantage of the imaging-reconstruction approach lies in its ability to produce also spatially resolved porosities. This allows us to investigate radial and axial porosity distributions, that is, those perpendicular and parallel to the axis of the cylindrically confined monolith. The analysis of spatial anisotropies is important if a preferred direction for macroscopic fluid flow shall be realized, as needed when these polymers are applied in separation science, as flow-through reactors, in gas storage, and so on. The spatially resolved porosity analysis is summarized in Fig. 4. In the studied material, the polymer forms a dense layer with a thickness of a few micrometers at the capillary inner wall and then exhibits a slight but systematic increase in porosity toward the center of the cylindrical column, from a value of 0.689 at about 6 μm from the column wall, to a value of 0.712 after a distance of approximately 41 μm. This is a consequence of the free-radical polymerization procedure used for the preparation of the monolith, which is exothermic and therefore generates a temperature profile affecting the reaction kinetics [83,84]. Interestingly, this outer layer (~2 μm thickness) corresponds to about 8% of the total sample volume. It is therefore important to distinguish between the global mean porosity (0.687), referring to the whole synthesized structure, and the accessible void space, calculated as the porosity of the central monolith region without impermeable wall layer, which is higher (0.716).

In contrast to the systematic variation of porosity over the cylinder cross-section (radial porosity distribution), its variation along the cylinder axis (axial porosity distribution) is random and small, rarely exceeding 1%. The 2D color map for the porosity in Fig. 4 reveals generally smooth transitions between denser and looser regions in the monolith, except near the column center, where they seem to occur more abruptly. However, this is not a real structural feature and is caused by the fact that the volume, corresponding to a radial position over which the porosity is averaged, decreases rapidly toward the column center. Which volume do we therefore need to probe to receive a reliable porosity value? To answer this question, we used a simple approach and extracted cubic subvolumes of varying edge length (ranging from 300 nm to 57 μm) to calculate their porosity. For each edge length, this procedure was repeated with 10 subvolumes randomly chosen from the entire sample. The result is shown in Fig. 5. Whereas the mean porosities are all similar, their standard deviations vary strongly; with small-volume reconstructions of only a few micrometers edge length (a volume typically sampled in FIB-SEM) one may easily misrepresent sample porosity by finite-size effects. The straightforward procedure we applied to validate if a porosity value is asymptotic (and thus accurate or not) underlines the importance of a carefully chosen sample volume.

Please cite this article in press as: T. Müllner, et al., Mater. Today (2014), http://dx.doi.org/10.1016/j.mattod.2014.07.003

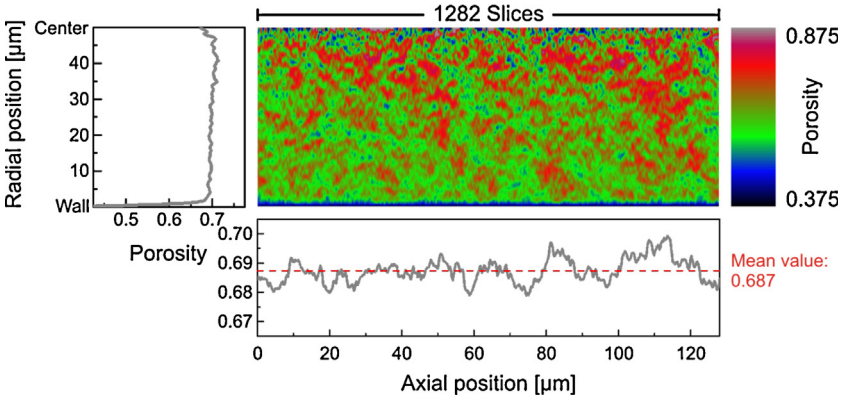

FIGURE 4

The imaging-reconstruction approach allows to analyze local porosity (interstitial void volume fraction) in the reconstructed cylindrical monolith segment. The color map represents porosity averaged over each radial position, for each of the 1282 imaged slices. The radially averaged axial porosity profile shown at the bottom is essentially flat and reveals only minor, random variations (~1%), whereas the axially averaged radial porosity profile to the left contains two distinct features: (i) a drop near the wall reflecting a dense polymer layer of ca. 2 µm thickness, and (ii) a slight, systematic increase beyond that layer toward the center of the monolith.

Chord length distributions

The analysis of global porosity is a relatively simple task and a 3D reconstruction is seldom necessary to determine this parameter. A locally resolved porosity analysis provides already deeper insight into systematic or stochastic variations of porosity compared to a global porosity estimate, which may be related to the conditions used for synthesis of a material. However, this is not sufficient to evaluate and compare the morphologies of different materials. A good method for characterization should provide several properties. First, it should make no assumption about the pore shape and size distribution, as this allows for universality in a comparison of different morphologies [85]. Second, the method should be unambiguous with respect to its application and easily automatable, to limit bias from the user. Further, it should be possible to extract simple measures for statistically relevant structural features and to relate them to transport properties, which often lies at the heart of an application.

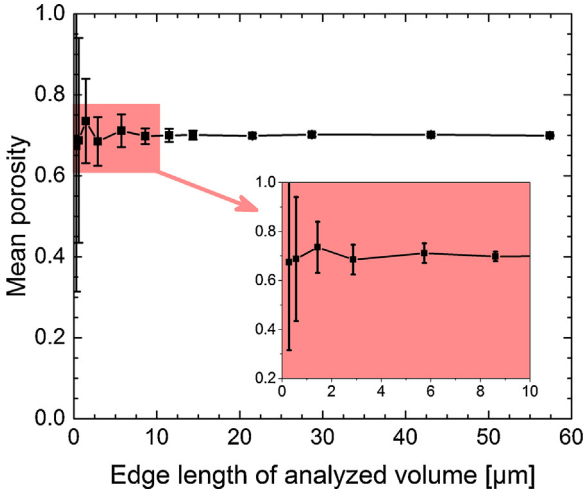

FIGURE 5

Finite-size effects on the determination of mean porosity. Each data point represents the average from 10 cubic subvolumes of the indicated edge length, randomly distributed over the entire reconstruction. While the first statistical moment shows no systematic variation with decreasing edge length, the second statistical moment increases drastically.

An approach that meets these criteria uses chord length distributions (CLDs) [73,86–90]. Applicable to any porous material representation that allows the unequivocal distinction between solid and void space, the CLD approach provides accurate results because it neither makes nor requires assumptions about the geometry of the pore space inherent to bulk methods such as mercury intrusion porosimetry and nitrogen physisorption. A CLD for the interstitial void space of the monolith, for example, is obtained by scanning the solid-void border with chords and collecting the resulting straight, skeleton-to-skeleton distances (chord lengths) in a histogram that lists the relative frequency of each chord length, as illustrated in Fig. 6. Chords are generated by randomly choosing points in the void space and projecting pairs of opposing vectors from this point in several directions until they strike the solid skeleton of the monolith (vectors projecting out of the image border are discarded). The distance spanned by a vector pair is a chord length. Since points can be generated in either the pores or the skeleton of the monolith CLD analysis is a powerful statistical method to describe the void space as well as the solid phase of porous materials [91].

The resulting histograms (containing ~10^6 chords, Fig. 6) can be evaluated using simple descriptive statistics, returning the mean characteristic length and (normalized) variance, or by fitting an appropriate function. For example, this is an exponential decay function for materials with Debye randomness [92]. For materials featuring correlated disorder, as in this study, a two-parameter k, Γ-function based on a statistical mechanics approach to characterize volume fluctuations in random porous media [93] can be fitted to the CLDs [85,94–96]:

$$f(l_c) = \frac{k^k}{\Gamma(k)} \frac{l_c^{k-1}}{\mu^k} \exp\left(-k\frac{l_c}{\mu}\right) \quad (1)$$

In eqn 1, l_c denotes chord length, µ is the first statistical moment of the distribution, $k = \mu^2/\sigma^2$ relates first (µ) and second (σ) statistical moments of the distribution, and Γ is the gamma function. k is a measure for microstructural heterogeneity over a distance of a few pores [96], which distinguishes random from ordered materials. Lower k-values represent a wider distribution relative to µ, thus, a larger heterogeneity. An interesting feature revealed by the CLD

Please cite this article in press as: T. Müllner, et al., Mater. Today (2014), http://dx.doi.org/10.1016/j.mattod.2014.07.003

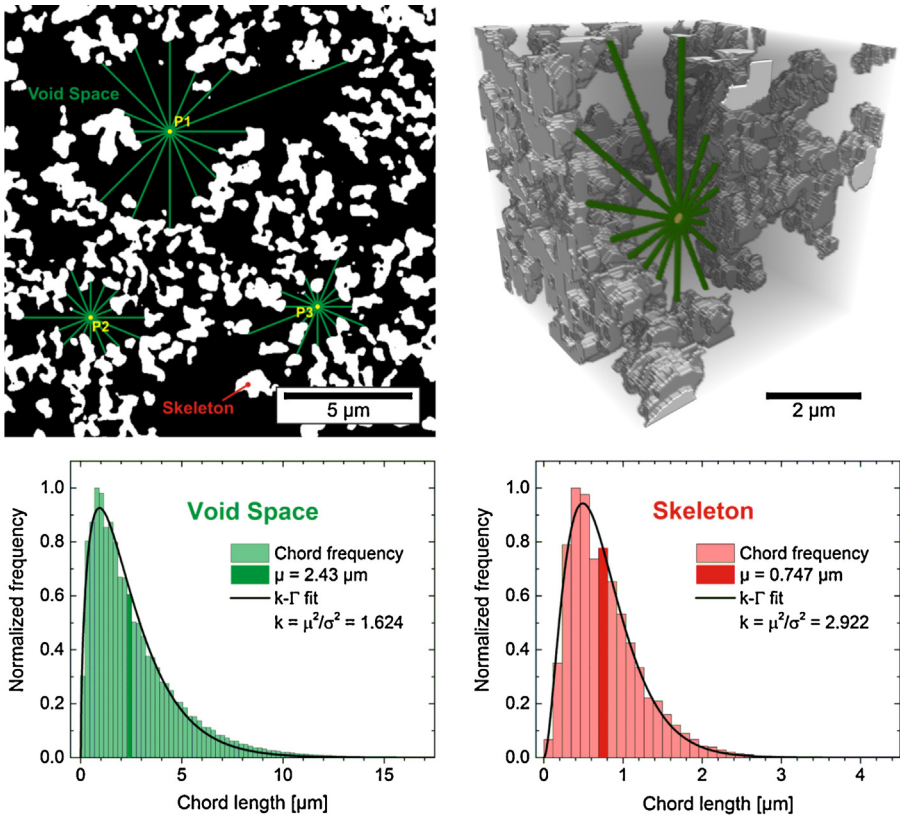

FIGURE 6

Chord length distribution (CLD) analysis for the investigation of void space and skeleton characteristic sizes as well as their heterogeneities. Chords are generated by randomly choosing points, for example in the interstitial void space of the monolith (top left panel), and projecting pairs of opposing vectors from these points equiangularly in several directions until they hit the solid skeleton (cf. green lines). The distance spanned by a vector pair is a chord length. A 3D representation is shown in the top right panel. Chords for the void space and skeleton can be stacked to give the respective CLDs (bottom panels), which are then fitted to eqn 1 (black lines), returning a descriptor for mean size (µ) and heterogeneity (*k*).

analysis (Fig. 6) is the structural independence of skeleton and void space. The void space has a global mean characteristic length of $\mu_{gl,void} = 2.43$ µm (extracted from the best fit of eqn 1 to the CLD generated in the entire void space), together with a global heterogeneity characterized by $k_{gl,void} = 1.62$. The skeleton on the other hand has a much smaller $\mu_{gl,skel} = 0.75$ µm and is relatively homogeneous ($k_{gl,skel} = 2.9$).

The comparison between these parameter values is only justified if finite-size effects are absent. To clarify this point, we followed the same approach as with the porosity: CLDs were generated and analyzed for subvolumes of varying edge length (10 subvolumes for each edge length) chosen randomly from the entire reconstruction. The results of this evaluation are summarized in Fig. 7. Unsurprisingly, the asymptotic value for the mean characteristic length is earlier reached for the skeleton (μ_{skel}) than for the void space (μ_{void}), because the latter is about three times larger (see left panels in Fig. 7). A similar behavior is observed for the parameter *k*, which reaches its asymptotic value earlier for the skeleton than for the more heterogeneous void space (right panels in Fig. 7). It is important to distinguish between the impact of finite-size effects on porosity (discussed above) and on the current CLD analysis. While the porosity still has the correct mean value when a sufficient number of samples is investigated and only the variance of evaluated porosities increases with smaller subvolumes, in the CLD analysis the finite-size effects influence the mean values of µ and *k* as well as their variance. To summarize, only the second statistical moment is finite-size dependent in the porosity analysis, whereas in the CLD analysis first and second statistical moments are sensitive to the size of the probed sample volume.

An intriguing representation of all the data in a single graph is achieved by the use of normalized parameters, as shown in Fig. 8. Edge length is normalized by $\mu_{gl,void}$ and $\mu_{gl,skel}$ for void space and skeleton, respectively, and µ and *k* are similarly normalized by their global values (see legend of Fig. 8). All curves in this dimensionless plot demonstrate a similar behavior and reach their asymptotic values for an edge length of 20–25 times the respective mean characteristic length. Consequently, we recommend a simple procedure to determine the minimal representative volume for CLD analysis. In the first step, the mean characteristic length of the largest feature of interest (e.g., pore size) is estimated using a fast method such as conventional SEM. Then, a reconstruction should be acquired that covers a volume equivalent to a cube with an edge length of ~25 times the estimated mean characteristic length. Thus, with a material for which the feature has a mean characteristic length of just 2 µm, a reconstructed volume of 40–50 µm edge length is already necessary. This may exceed the capabilities of FIB-SEM, especially if feature sizes become larger. The SBF-SEM approach introduced at the beginning of this paper offers an alternative technique, which provides the required large-volume reconstructions to conduct a meaningful morphological analysis.

Please cite this article in press as: T. Müllner, et al., Mater. Today (2014), http://dx.doi.org/10.1016/j.mattod.2014.07.003

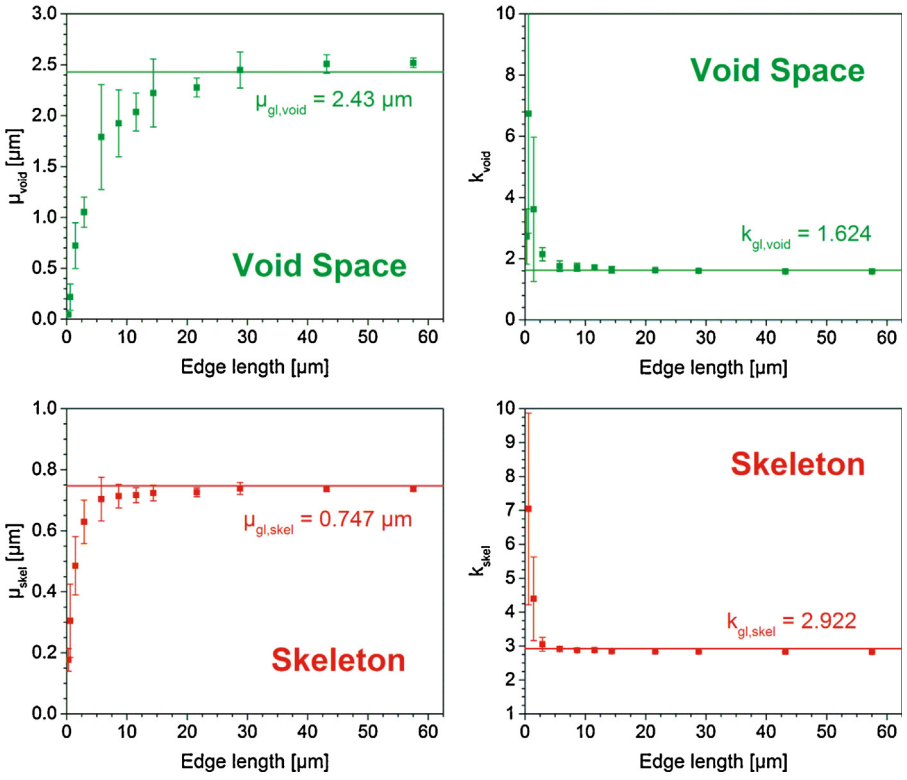

FIGURE 7

Finite-size effects in the CLD analysis of void space (top panels) and skeleton (bottom panels). Cubic subvolumes of defined edge length (10 subvolumes for each edge length) are randomly chosen from the entire sample to perform a CLD analysis. Parameters of the best fit of eqn 1 to the CLDs are then plotted vs. edge length. Insufficiently large reconstructions are significantly affected in their morphological parameters; while mean characteristic sizes (μ-values, left panels) are underestimated, the homogeneities are overestimated (*k*-values, right panels).

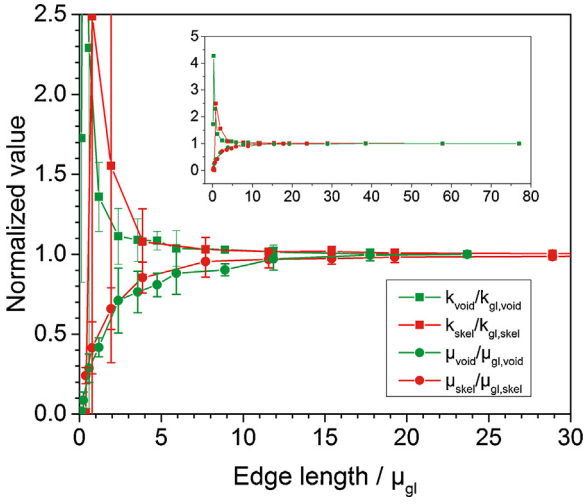

FIGURE 8

Normalized representation of finite-size effects on the morphological parameters extracted from the CLD analysis of void space and skeleton. Edge length is normalized by $\mu_{gl,void}$ ($\mu_{gl,skel}$) for void space (skeleton), and μ and *k* are similarly normalized by their respective global values. All normalized parameters converge to their asymptotic values for analyzed volumes having an edge length of 20–25 times the respective global mean feature size (μ_{gl}).

Concluding remarks

We have shown that image analysis based on SBF-SEM delivers an accurate characterization of micron and submicron morphological features of porous polymeric materials. SBF-SEM is a promising method for that purpose and has been used to reconstruct a 100 μm diameter, ca. 130 μm long specimen from a laboratory sample of a hypercrosslinked poly(styrene-divinylbenzene) monolith. The reconstruction allowed us to quantify finite-size effects on the determination of key structural parameters relevant to mass transport in the monolith. The approach enables materials scientists to identify and improve morphological features behind the performance of a material to achieve optimal results. These reconstructions will also serve as realistic 3D models in simulations of flow, mass transport, sorption, and reaction, to quantify morphology-transport relationships for materials with important technological or environmental background [97].

Acknowledgement

We thank Dr Yongqin Lv for providing the hypercrosslinked poly(styrene-divinylbenzene) monolith and Claudia Mayrhofer for assistance with conventional ultramicrotomy for sample preparation.

References

[1] D. Astruc, et al. Angew. Chem. Int. Ed. 44 (2005) 7852, http://dx.doi.org/10.1002/anie.200500766.
[2] A.-H. Lu, et al. Angew. Chem. Int. Ed. 46 (2007) 1222, http://dx.doi.org/10.1002/anie.200602866.
[3] J. Delerue, et al. Phys. Chem. Earth, Part A Solid Earth Geod. 24 (1999) 639, http://dx.doi.org/10.1016/S1464-1895(99)00093-9.
[4] H.-J. Vogel, K. Roth, J. Hydrol. 272 (2003) 95, http://dx.doi.org/10.1016/S0022-1694(02)00257-3.

Please cite this article in press as: T. Müllner, et al., Mater. Today (2014), http://dx.doi.org/10.1016/j.mattod.2014.07.003

[5] W.D. Carlson, Earth Planet. Sci. Lett. 249 (2006) 133, http://dx.doi.org/10.1016/j.epsl.2006.06.020.
[6] P. Levitz, Cem. Concr. Res. 37 (2007) 351, http://dx.doi.org/10.1016/j.cemconres.2006.08.004.
[7] M. Dentz, et al. J. Contam. Hydrol. 120–121 (2011), http://dx.doi.org/10.1016/j.jconhyd.2010.05.0021.
[8] O. Rozenbaum, et al. Comptes Rendus Geosci. 344 (2012) 516, http://dx.doi.org/10.1016/j.crte.2012.09.004.
[9] J. Rzayev, M.A. Hillmyer, J. Am. Chem. Soc. 127 (2005) 13373, http://dx.doi.org/10.1021/ja053731d.
[10] W.H. Binder, R. Sachsenhofer, Macromol. Rapid Commun. 28 (2007) 15, http://dx.doi.org/10.1002/marc.200600625.
[11] A. Stein, et al. Adv. Mater. 21 (2009) 265, http://dx.doi.org/10.1002/adma.200801492.
[12] T. Muller, S. Bräse, Angew. Chem. Int. Ed. 50 (2011) 11844, http://dx.doi.org/10.1002/anie.201105707.
[13] F. Svec, J. Chromatogr. A 1217 (2010) 902, http://dx.doi.org/10.1016/j.chroma.2009.09.073.
[14] W. Li, et al. Chem. Mater. 17 (2005) 3620, http://dx.doi.org/10.1021/cm050345m.
[15] A. Thomas, et al. Chem. Mater. 20 (2008) 738, http://dx.doi.org/10.1021/cm702126j.
[16] R. Dawson, et al. Prog. Polym. Sci. 37 (2012) 530, http://dx.doi.org/10.1016/j.progpolymsci.2011.09.002.
[17] D. Wu, et al. Chem. Rev. 112 (2012) 3959, http://dx.doi.org/10.1021/cr200440z.
[18] M. Oschatz, et al. Angew. Chem. Int. Ed. 51 (2012) 7577, http://dx.doi.org/10.1002/anie.201200024.
[19] H. Sai, et al. Science 341 (2013) 530, http://dx.doi.org/10.1126/science.1238159.
[20] F. Schüth, Annu. Rev. Mater. Res. 35 (2005) 209, http://dx.doi.org/10.1146/annurev.matsci.35.012704.142050.
[21] A. El Kadib, et al. Angew. Chem. Int. Ed. 48 (2009) 4969, http://dx.doi.org/10.1002/anie.200805580.
[22] C.M.A. Parlett, et al. Chem. Soc. Rev. 42 (2013) 3876, http://dx.doi.org/10.1039/c2cs35378d.
[23] D.H. Kim, S.C. Kim, Macromol. Res. 16 (2008) 457, http://dx.doi.org/10.1007/BF03218545.
[24] H. Schulenburg, et al. J. Phys. Chem. C 115 (2011) 14236, http://dx.doi.org/10.1021/jp203016u.
[25] P. Novák, et al. Chem. Rev. 97 (1997) 207, http://dx.doi.org/10.1021/cr941181o.
[26] C.L. Cheng, et al. J. Power Sources 134 (2004) 202, http://dx.doi.org/10.1016/j.jpowsour.2004.03.037.
[27] Y.J. Hwang, et al. J. Membr. Sci. 310 (2008) 349, http://dx.doi.org/10.1016/j.memsci.2007.11.006.
[28] F. Vilela, et al. Energy Environ. Sci. 5 (2012) 7819, http://dx.doi.org/10.1039/c2ee22002d.
[29] D. Wei, et al. Nano Energy 2 (2013) 1054, http://dx.doi.org/10.1016/j.nanoen.2013.04.004.
[30] J.F. Mike, J.L. Lutkenhaus, ACS Macro Lett. 2 (2013) 839, http://dx.doi.org/10.1021/mz400329j.
[31] F. Svec, J. Sep. Sci. 27 (2004) 1419, http://dx.doi.org/10.1002/jssc.200401825.
[32] M.J. Benes, et al. J. Sep. Sci. 28 (2005) 1855, http://dx.doi.org/10.1002/jssc.200500186.
[33] F. Svec, J. Sep. Sci. 32 (2009) 3, http://dx.doi.org/10.1002/jssc.200800530.
[34] J. Germain, et al. Small 5 (2009) 1098, http://dx.doi.org/10.1002/smll.200801762.
[35] H. Ostadi, et al. J. Membr. Sci. 351 (2010) 69, http://dx.doi.org/10.1016/j.memsci.2010.01.031.
[36] M. Kaliva, et al. Langmuir 28 (2012) 2690, http://dx.doi.org/10.1021/la204991n.
[37] T.M. Madkour, J.E. Mark, J. Membr. Sci. 431 (2013) 37, http://dx.doi.org/10.1016/j.memsci.2012.12.033.
[38] G. Wang, et al. Chem. Eng. Sci. 62 (2007) 5110, http://dx.doi.org/10.1016/j.ces.2007.01.046.
[39] K. Zhu, et al. Nano Res. 2 (2010) 1, http://dx.doi.org/10.1007/s12274-009-9002-2.
[40] F. Tariq, et al. Chem. Eng. Sci. 66 (2011) 5804, http://dx.doi.org/10.1016/j.ces.2011.07.034.
[41] M.J. Blunt, et al. Adv. Water Resour. 51 (2013) 197, http://dx.doi.org/10.1016/j.advwatres.2012.03.003.
[42] A.P. Cocco, et al. Phys. Chem. Chem. Phys. 15 (2013) 16377, http://dx.doi.org/10.1039/c3cp52356j.
[43] G. Möbus, B.J. Inkson, Mater. Today 10 (2007) 18, http://dx.doi.org/10.1016/S1369-7021(07)70304-8.
[44] S. Attinger, et al. Stoch. Environ. Res. Risk Assess. 18 (2004) 9, http://dx.doi.org/10.1007/s00477-003-0160-6.
[45] A. Daneyko, et al. J. Chromatogr. A 1218 (2011) 8231, http://dx.doi.org/10.1016/j.chroma.2011.09.039.
[46] A. Daneyko, et al. J. Chromatogr. A 1257 (2012) 98, http://dx.doi.org/10.1016/j.chroma.2012.08.024.
[47] E.A. Wargo, et al. J. Power Sources 241 (2013) 608, http://dx.doi.org/10.1016/j.jpowsour.2013.04.153.
[48] L.R. Aramburo, et al. Angew. Chem. Int. Ed. 51 (2012) 3616, http://dx.doi.org/10.1002/anie.201109026.
[49] R. Leary, et al. Acc. Chem. Res. 45 (2012) 1782, http://dx.doi.org/10.1021/ar3001102.
[50] P.A. Midgley, M. Weyland, Ultramicroscopy 96 (2003) 413, http://dx.doi.org/10.1016/S0304-3991(03)00105-0.
[51] Z. Saghi, P.A. Midgley, Annu. Rev. Mater. Res. 42 (2012) 59, http://dx.doi.org/10.1146/annurev-matsci-070511-155019.
[52] D. Schryvers, et al. Sci. Technol. Adv. Mater. 14 (2013) 014206, http://dx.doi.org/10.1088/1468-6996/14/1/014206.
[53] G. Van Tendeloo, et al. Adv. Mater. 24 (2012) 5655, http://dx.doi.org/10.1002/adma.201202107.
[54] C.J. Peddie, L.M. Collinson, Micron 61 (2014) 9, http://dx.doi.org/10.1016/j.micron.2014.01.009.
[55] M.W. Phaneuf, in: L.A. Giannuzzi, F.A. Stevie (Eds.), Introduction to Focused Ion Beams: Instrumentation, Theory, Techniques and Practice, Springer, Boston, MA, 2005 (Chapter 8).
[56] J. Benawra, et al. J. Microsc. 234 (2009) 89, http://dx.doi.org/10.1111/j.1365-2818.2009.03151.x.
[57] N. Vivet, et al. J. Power Sources 196 (2011) 7541, http://dx.doi.org/10.1016/j.jpowsour.2011.03.060.
[58] M. Vázquez, et al. Analyst 139 (2014) 99, http://dx.doi.org/10.1039/c3an01827j.
[59] A. Sheidaei, et al. Compos. Sci. Technol. 80 (2013) 47, http://dx.doi.org/10.1016/j.compscitech.2013.03.001.
[60] T. Hutzenlaub, et al. Electrochem. Commun. 27 (2013) 77, http://dx.doi.org/10.1016/j.elecom.2012.11.006.
[61] L. Karwacki, et al. Angew. Chem. Int. Ed. 50 (2011) 1294, http://dx.doi.org/10.1002/anie.201006031.
[62] P. Levitz, Adv. Colloid Interface Sci. 76–77 (1998) 71, http://dx.doi.org/10.1016/S0001-8686(98)00042-6.
[63] T. Kanit, et al. Int. J. Solids Struct. 40 (2003) 3647, http://dx.doi.org/10.1016/S0020-7683(03)00143-4.
[64] S.K. Matthäi, Geophys. Res. Lett. 31 (2004) L07602, http://dx.doi.org/10.1029/2003GL019027.
[65] E.A. Wargo, et al. J. Power Sources 197 (2012) 168, http://dx.doi.org/10.1016/j.jpowsour.2011.09.035.
[66] W. Denk, H. Horstmann, PLoS Biol. 2 (2004) e329, http://dx.doi.org/10.1371/journal.pbio.0020329.
[67] A. Zankel, et al. J. Microsc. 233 (2009) 140, http://dx.doi.org/10.1111/j.1365-2818.2008.03104.x.
[68] E.I. Trilisky, et al. J. Chromatogr. A 1216 (2009) 6365, http://dx.doi.org/10.1016/j.chroma.2009.07.005.
[69] H. Reingruber, et al. J. Membr. Sci. 372 (2011) 66, http://dx.doi.org/10.1016/j.memsci.2011.01.037.
[70] H. Koku, et al. J. Chromatogr. A 1218 (2011) 3466, http://dx.doi.org/10.1016/j.chroma.2011.03.064.
[71] B. Chen, et al. Sci. Rep. 3 (2013) 1177, http://dx.doi.org/10.1038/srep01177.
[72] J. Urban, et al. J. Chromatogr. A 1217 (2010) 8212, http://dx.doi.org/10.1016/j.chroma.2010.10.100.
[73] J. Courtois, et al. Anal. Chem. 79 (2007) 335, http://dx.doi.org/10.1021/ac0614902.
[74] D. Hlushkou, et al. Anal. Chem. 82 (2010) 7150, http://dx.doi.org/10.1021/ac101393b.
[75] Y. Fang, et al. J. Chromatogr. A 1217 (2010) 6405, http://dx.doi.org/10.1016/j.chroma.2010.08.026.
[76] K. Schmidt, J. Becker, Adv. Eng. Mater. 15 (2013) 40, http://dx.doi.org/10.1002/adem.201200097.
[77] S. Diamond, Cem. Concr. Res. 30 (2000) 1517, http://dx.doi.org/10.1016/S0008-8846(00)00370-7.
[78] H. Saito, et al. J. Chromatogr. A 1119 (2006) 95, http://dx.doi.org/10.1016/j.chroma.2006.03.087.
[79] H.J. Castelijns, et al. J. Appl. Phys. 102 (2007) 114901, http://dx.doi.org/10.1063/1.2817577.
[80] C.R. López-Barrón, C.W. Macosko, J. Microsc. 242 (2011) 242, http://dx.doi.org/10.1111/j.1365-2818.2010.03462.x.
[81] J. Rouquerol, et al. Microporous Mesoporous Mater. 154 (2012) 2, http://dx.doi.org/10.1016/j.micromeso.2011.09.031.
[82] A.H. Dessources, et al. J. Mater. Chem. 22 (2012) 2713, http://dx.doi.org/10.1039/c1jm14905a.

Please cite this article in press as: T. Müllner, et al., Mater. Today (2014), http://dx.doi.org/10.1016/j.mattod.2014.07.003

[83] C. Viklund, et al. Chem. Mater. 8 (1996) 744, http://dx.doi.org/10.1021/cm950437j.
[84] F. Svec, J.M.J. Frechet, Macromolecules 28 (1995) 7580, http://dx.doi.org/10.1021/ma00126a044.
[85] S. Bruns, et al. LCGC North Am. 31 (2013) 486.
[86] B. Lu, S. Torquato, J. Chem. Phys. 98 (1993) 6472, http://dx.doi.org/10.1063/1.464812.
[87] W. Gille, et al. J. Porous Mater. 9 (2002) 221, http://dx.doi.org/10.1023/A:1020943119268.
[88] B. Smarsly, et al. J. Chem. Phys. 116 (2002) 2618, http://dx.doi.org/10.1063/1.1433463.
[89] M. Pons, et al. Chem. Eng. Sci. 61 (2006) 3962, http://dx.doi.org/10.1016/j.ces.2006.01.036.
[90] K. Schladitz, et al. Methodol. Comput. Appl. Probab. 14 (2011) 1011, http://dx.doi.org/10.1007/s11009-010-9208-5.
[91] S. Bruns, et al. Anal. Chem. 82 (2010) 6569, http://dx.doi.org/10.1021/ac100909t.
[92] S. Torquato, Random Heterogeneous Materials: Microstructure and Macroscopic Properties, Springer, New York, NY, 2002.
[93] T. Aste, T. Di Matteo, Phys. Rev. E 77 (2008) 021309, http://dx.doi.org/10.1103/PhysRevE.77.021309.
[94] I. Schenker, et al. Phys. Rev. E 80 (2009) 021302, http://dx.doi.org/10.1103/PhysRevE.80.021302.
[95] K. Hormann, et al. J. Chromatogr. A 1222 (2012) 46, http://dx.doi.org/10.1016/j.chroma.2011.12.008.
[96] K. Hormann, U. Tallarek, J. Chromatogr. A 1312 (2013) 26, http://dx.doi.org/10.1016/j.chroma.2013.08.087.
[97] D. Hlushkou, et al. J. Chromatogr. A 1303 (2013) 28, http://dx.doi.org/10.1016/j.chroma.2013.06.039.

Please cite this article in press as: T. Müllner, et al., Mater. Today (2014), http://dx.doi.org/10.1016/j.mattod.2014.07.003